

Exposing unsaturated Cu¹-O₂ sites in nanoscale Cu-MOF for efficient electrocatalytic hydrogen evolution

Cheng, Weiren; Zhang, Huabin; Luan, Deyan; Lou, David Xiong Wen

2021

Cheng, W., Zhang, H., Luan, D. & Lou, D. X. W. (2021). Exposing unsaturated Cu¹-O₂ sites in nanoscale Cu-MOF for efficient electrocatalytic hydrogen evolution. *Science Advances*, 7(18), eabg2580-. <https://dx.doi.org/10.1126/sciadv.abg2580>

<https://hdl.handle.net/10356/151046>

<https://doi.org/10.1126/sciadv.abg2580>

© 2021 The Authors, some rights reserved; exclusive licensee American Association for the Advancement of Science. No claim to original U.S. Government Works. Distributed under a Creative Commons Attribution NonCommercial License 4.0 (CC BY-NC).

Downloaded on 26 Aug 2022 23:42:48 SGT

MATERIALS SCIENCE

Exposing unsaturated Cu₁-O₂ sites in nanoscale Cu-MOF for efficient electrocatalytic hydrogen evolution

Weiren Cheng, Huabin Zhang, Deyan Luan, Xiong Wen (David) Lou*

Conductive metal-organic framework (MOF) materials have been recently considered as effective electrocatalysts. However, they usually suffer from two major drawbacks, poor electrochemical stability and low electrocatalytic activity in bulk form. Here, we have developed a rational strategy to fabricate a promising electrocatalyst composed of a nanoscale conductive copper-based MOF (Cu-MOF) layer fully supported over synergetic iron hydr(oxy)oxide [Fe(OH)_x] nanoboxes. Owing to the highly exposed active centers, enhanced charge transfer, and robust hollow nanostructure, the obtained Fe(OH)_x@Cu-MOF nanoboxes exhibit superior activity and stability for the electrocatalytic hydrogen evolution reaction (HER). Specifically, it needs an overpotential of 112 mV to reach a current density of 10 mA cm⁻² with a small Tafel slope of 76 mV dec⁻¹. X-ray absorption fine structure spectroscopy combined with density functional theory calculations unravels that the highly exposed coordinatively unsaturated Cu₁-O₂ centers could effectively accelerate the formation of key *H intermediates toward fast HER kinetics.

INTRODUCTION

Green hydrogen generation through electrochemical water reduction has been regarded as a promising approach for effective conversion and storage of renewable energy sources toward addressing the global energy and environmental issues (1–4). Nowadays, industrial electric-driven water reduction for hydrogen production is mainly based on alkaline electrolyzer cells, where the half reaction of hydrogen evolution reaction (HER) encounters substantially sluggish kinetics due to the large activation barrier of H–O bonds of water molecules (5, 6). To date, platinum (Pt)-based materials have been considered as the most active and stable HER catalysts in the commercial electrolyzer cells, but their scarcity and high cost hamper the scaling up for practical hydrogen production (7, 8). Therefore, it is highly urgent to seek active, stable, and earth-abundant alternatives to Pt-based catalysts toward efficient electrochemical hydrogen evolution in alkaline media (9–12).

Conductive metal-organic frameworks (MOFs), with dispersed planar metal nodes and unique two-dimensional π -conjugated structures (13–15), have been intensively reported as potential promising electrocatalysts toward hydrogen evolution (16–18), oxygen evolution and reduction (19, 20), electric energy storage (21, 22), and so on. Despite fast charge transfer behaviors, conductive MOF in bulk generally has limited redox capability and moderate HER activity, due to the coordinatively saturated metal nodes and small amount of exposed active sites (23, 24). In addition, self-standing ultrathin conductive MOF nanosheets with highly exposed active sites are usually synthesized through a precisely controlled liquid-liquid or air-liquid reaction, which is generally very challenging and has low yield (25, 26). Furthermore, the assembled electrodes of ultrathin conductive MOF nanosheets could suffer from serious delamination problems when the precursor and/or product bubbles permeate between the stacking interlayers during the electrocatalytic processes (23, 27). To overcome these issues, anchoring an ultrathin layer of conductive MOF with highly exposed active metal centers onto a robust well-designed scaffold would be an effective resolution.

Recently, hollow nanostructures of transition-metal oxides and/or hydr(oxy)oxides with high specific surface areas and robust structural properties have been commonly regarded as useful architectural scaffolds for accommodation of abundant surface active sites (28–31). Accordingly, rational design of a hollow nanostructure, composed of ultrathin MOF outer skin and robust transition-metal hydr(oxy)oxide inner shell, will be intuitively beneficial for improving the intrinsic electrocatalytic activity and structural stability of conductive MOF toward efficient electrochemical water reduction.

Here, we report the delicate design and synthesis of an ultrathin layer of conductive copper-based MOF (Cu-MOF) fully supported on the surface of iron hydr(oxy)oxide [Fe(OH)_x] nanoboxes (NBs) [designated as Fe(OH)_x@Cu-MOF] by a facile template-engaged solvothermal reaction and subsequent redox-etching strategy. The X-ray absorption fine structure (XAFS) spectroscopy and X-ray photoelectron spectroscopy (XPS) analyses reveal the abundance of coordinatively unsaturated Cu₁-O₂ centers in these Fe(OH)_x@Cu-MOF NBs. With the highly exposed active Cu centers and the well-designed architecture, the synthesized Fe(OH)_x@Cu-MOF NBs exhibit excellent HER activity and stability in alkaline solution, with an overpotential of 112 mV at 10 mA cm⁻² and a small Tafel slope of 76 mV dec⁻¹, thus among the best MOF-based HER electrocatalysts reported so far. Density functional theory (DFT) calculations unveil that the local electronic polarization of unsaturated Cu₁-O₂ centers in the Cu-MOF outer layer is essentially helpful for promoting the formation of adsorbed *H intermediates, thus enhancing greatly the HER kinetics.

RESULTS

Synthesis and structural characterization

The overall synthesis route of Fe(OH)_x@Cu-MOF NBs is schematically illustrated in Fig. 1. The uniform Cu₂O nanocubes with an average size of about 900 nm (figs. S1 to S3) are used as the starting material. Initially, these Cu₂O nanocubes undergo a solvothermal reaction for the surface growth of a layer of conductive Cu-MOF with 2,3,6,7,10,11-hexahydroxytriphenylene (HHTP) molecules as the organic linkers. During this solvothermal reaction, the Cu₂O nanocubes are locally dissolved to release copper cations, accompanied

Copyright © 2021
The Authors, some
rights reserved;
exclusive licensee
American Association
for the Advancement
of Science. No claim to
original U.S. Government
Works. Distributed
under a Creative
Commons Attribution
NonCommercial
License 4.0 (CC BY-NC).

School of Chemical and Biomedical Engineering, Nanyang Technological University, 62 Nanyang Drive, Singapore 637459, Singapore.

*Corresponding author. Email: xwlou@ntu.edu.sg

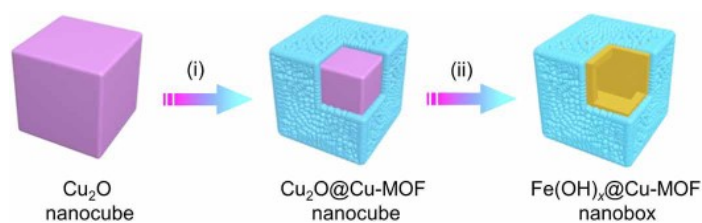


Fig. 1. Schematic illustration of the synthetic process for Fe(OH)_x@Cu-MOF NB.

(i) Growth of a conductive Cu-MOF layer over Cu₂O nanocube via the reaction of locally dissolved Cu ions with organic ligands during the solvothermal process. (ii) Conversion to Fe(OH)_x@Cu-MOF NB through a subsequent redox-etching process, where the exact value of subscript *x* in Fe(OH)_x is undetermined but rather suggests the amorphous nature of the inner Fe(OH)_x layer in Fe(OH)_x@Cu-MOF NB.

by rapid nucleation of Cu-MOF on the surface, generating well-defined Cu₂O@Cu-MOF core-shell nanocubes. Subsequently, the inner Cu₂O core of the obtained Cu₂O@Cu-MOF nanocubes is selectively removed through a facile redox-etching approach in the presence of Fe³⁺ ions. During this oxidative etching process, a thin Fe(OH)_x shell is gradually precipitated underneath the surface Cu-MOF layer (32), finally producing well-defined Fe(OH)_x@Cu-MOF NBs.

Field-emission scanning electron microscopy (FESEM) images (Fig. 2, A and B, and fig. S4) and transmission electron microscopy (TEM) images (Fig. 2, C and D, and fig. S5) show a Cu-MOF layer fully covering over the surface of Cu₂O in the Cu₂O@Cu-MOF nanocubes after the solvothermal reaction. X-ray diffraction (XRD) analysis (fig. S6, A and B) confirms the coexistence of hexagonal Cu-MOF and cubic Cu₂O (Joint Committee on Powder Diffraction Standards card no. 05-0667) in the Cu₂O@Cu-MOF core-shell nanocubes (22, 33, 34). Specifically, the two relatively weak diffraction peaks at 9.47° and 12.61° are well assigned to the (200) and (210) planes of hexagonal Cu-MOF, respectively, while those positioned at 29.51°, 36.39°, 42.36°, and 61.41° are well indexed to the (110), (111), (200), and (220) planes of cubic Cu₂O, respectively. These Cu₂O@Cu-MOF nanocubes are transformed into Fe(OH)_x@Cu-MOF NBs after a redox-etching process. FESEM images (Fig. 2, E and F, and fig. S7) show Fe(OH)_x@Cu-MOF NBs with a size of about 1 μm. Furthermore, TEM observations (Fig. 2, G and H, and fig. S8) elucidate an ultrathin Cu-MOF layer with a thickness of about 20 nm, fully supported over the surface of each Fe(OH)_x shell. The XRD pattern (fig. S9A) and Fourier transform infrared (FTIR) spectra (fig. S10) of Fe(OH)_x@Cu-MOF NBs further reveal the amorphous nature of Fe(OH)_x and the complete removal of Cu₂O. The high-angle annular dark-field scanning TEM (HAADF-STEM) and corresponding energy-dispersive X-ray (EDX) spectroscopy elemental mapping images (Fig. 2I) show that the Cu-MOF outer layer is tightly supported atop the surface of the Fe(OH)_x shell in Fe(OH)_x@Cu-MOF NBs, with a Cu:Fe molar ratio of about 0.34:1 (fig. 9B), which is close to the inductively coupled plasma-optical emission spectroscopy (ICP-OES) result (0.31:1). There are abundant mesopores mainly in the size range of 10 to 40 nm in Fe(OH)_x@Cu-MOF NBs, contributing to a relatively high specific surface area of about 293 m² g⁻¹ (fig. S11). On the basis of the aforementioned morphological and structural analyses, Fe(OH)_x@Cu-MOF NBs are successfully synthesized. For comparison, Fe(OH)_x NBs (figs. S12 and S13) and Cu-MOF nanoparticles (Cu-MOF NPs; figs. S14 and S15) were also prepared as two reference samples.

To explore the intrinsic atomic structure of Fe(OH)_x@Cu-MOF NBs, XAFS measurements were performed (35, 36). As can be seen from Fig. 3A, the *k*³χ(*k*) oscillation curve of Fe(OH)_x@Cu-MOF NBs at Cu *K*-edge shows a similar trend in shape and oscillating frequency to that of Cu-MOF NPs over the whole range of 2.0 to 12.0 Å⁻¹ and is obviously different from that of Cu₂O and CuO, inferring similar structural configurations of Cu nodes in both Fe(OH)_x@Cu-MOF NBs and Cu-MOF NPs. Furthermore, the Fourier transform curves of Cu *K*-edge extended XAFS (EXAFS) (Fig. 3B) show that only a dominant peak at about 1.50 Å, evidently contributed from the nearest coordination shell of Cu-O bonds (37, 38), is observed for both Fe(OH)_x@Cu-MOF NBs and Cu-MOF NPs. This suggests a dispersed planar Cu₁-O_x configuration of Cu nodes in both Fe(OH)_x@Cu-MOF NBs and Cu-MOF NPs (39, 40). Notably, Fe(OH)_x@Cu-MOF NBs show a weaker Cu-O peak relative to that of Cu-MOF NPs, possibly indicating the presence of partially coordinatively unsaturated Cu nodes. Moreover, the average oxidation state of Cu species in Fe(OH)_x@Cu-MOF NBs is confirmed as 1.7 based on the X-ray absorption near-edge spectra (XANES) analyses (fig. S16), obviously lower than that of Cu-MOF NPs (about 2), which again suggests the existence of unsaturated Cu nodes in Fe(OH)_x@Cu-MOF NBs. From the EXAFS fitting results (figs. S17 and S18 and table S1), the coordination number of Cu-O bonds is 4 for Cu-MOF NPs, indicating fully saturated Cu nodes of Cu₁-O₄ in Cu-MOF NPs. In comparison, the coordination number of Cu-O bonds of Fe(OH)_x@Cu-MOF NBs is quantitatively determined to be about 3.7, evidently confirming the coexistence of unsaturated Cu₁-O₂ and saturated Cu₁-O₄ centers.

In addition, a mixture phase of iron hydr(oxy)oxide and oxide is suggested for the Fe(OH)_x component of Fe(OH)_x@Cu-MOF NBs based on the *k*³χ(*k*) oscillation curves and Fourier transform results of Fe *K*-edge EXAFS (fig. S19) (41, 42). To clarify the electronic structure of Fe(OH)_x@Cu-MOF NBs, XPS characterizations were conducted (Fig. 3, C and D, and fig. S20). From the deconvolution results of Cu 2p shown in Fig. 3C, two dominant peaks are located at 932.6 and 934.5 eV for Fe(OH)_x@Cu-MOF NBs, which can be well assigned to the 2p_{3/2} of Cu⁺ and Cu²⁺ species, respectively (22, 37). These Cu⁺ and Cu²⁺ species may be derived from the unsaturated Cu₁-O₂ and saturated Cu₁-O₄ centers in Fe(OH)_x@Cu-MOF NBs, respectively. In consideration of an average valence state of Cu^{1.7+} species in Fe(OH)_x@Cu-MOF NBs as mentioned above, it is estimated to have about 30% of Cu species serving as unsaturated Cu₁-O₂ centers in Fe(OH)_x@Cu-MOF NBs. From the Fe 2p XPS spectra in Fig. 3D, two dominant peaks of 710.4 and 712.3 eV are observed for Fe(OH)_x@Cu-MOF NBs, which are ascribed to 2p_{3/2} of Fe²⁺ and Fe³⁺ species, respectively (42, 43). These XPS characterizations indicate the coexistence of various metal species of Cu^{+/2+} and Fe^{2+/3+} in Fe(OH)_x@Cu-MOF NBs. Accordingly, on the basis of the XAFS and XPS results, Fe(OH)_x@Cu-MOF NBs have abundant unsaturated Cu nodes as well as various metal species of Cu^{+/2+} and Fe^{2+/3+}, which would endow them with higher redox capability and electrocatalytic activity.

Electrocatalytic performance

To evaluate the electrocatalytic performance, electrochemical HER measurements were carried out in alkaline solution for Fe(OH)_x@Cu-MOF NBs, as well as Fe(OH)_x NBs, Cu-MOF NPs, and physical mixtures of Fe(OH)_x NBs and Cu-MOF NPs [designated as Fe(OH)_x + Cu-MOF] as references. Figure 4A depicts the linear sweep voltammetry

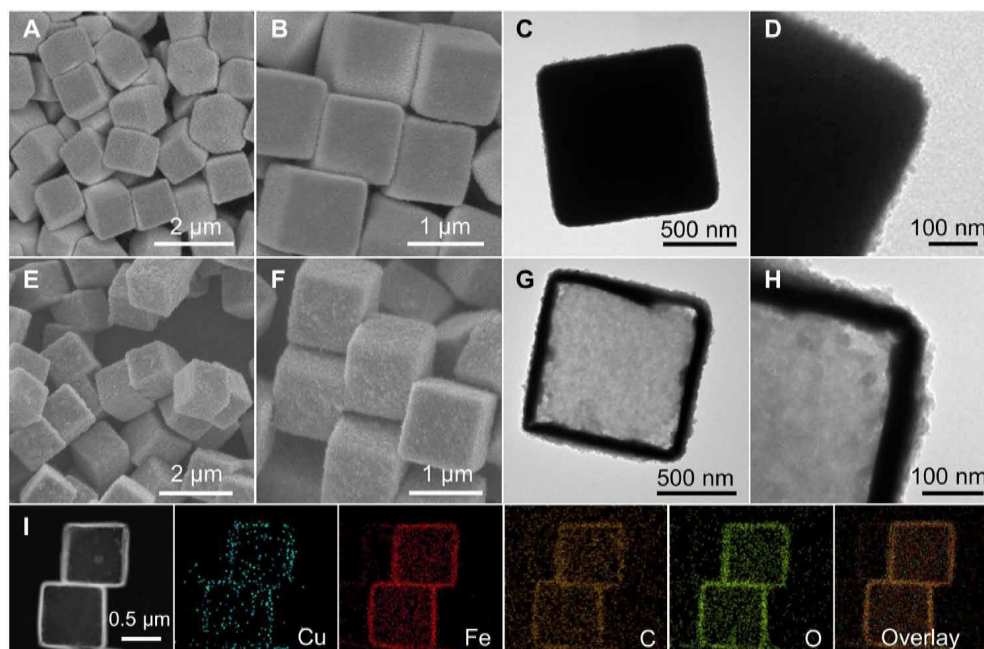


Fig. 2. Morphological and structural characterizations. (A and B) FESEM images of $\text{Cu}_2\text{O}@\text{Cu-MOF}$ nanocubes. (C and D) TEM images of $\text{Cu}_2\text{O}@\text{Cu-MOF}$ nanocubes. (E and F) FESEM images of $\text{Fe(OH)}_x@\text{Cu-MOF}$ NBs. (G and H) TEM images of $\text{Fe(OH)}_x@\text{Cu-MOF}$ NBs. (I) HAADF-STEM image and corresponding elemental mapping images of $\text{Fe(OH)}_x@\text{Cu-MOF}$ NBs.

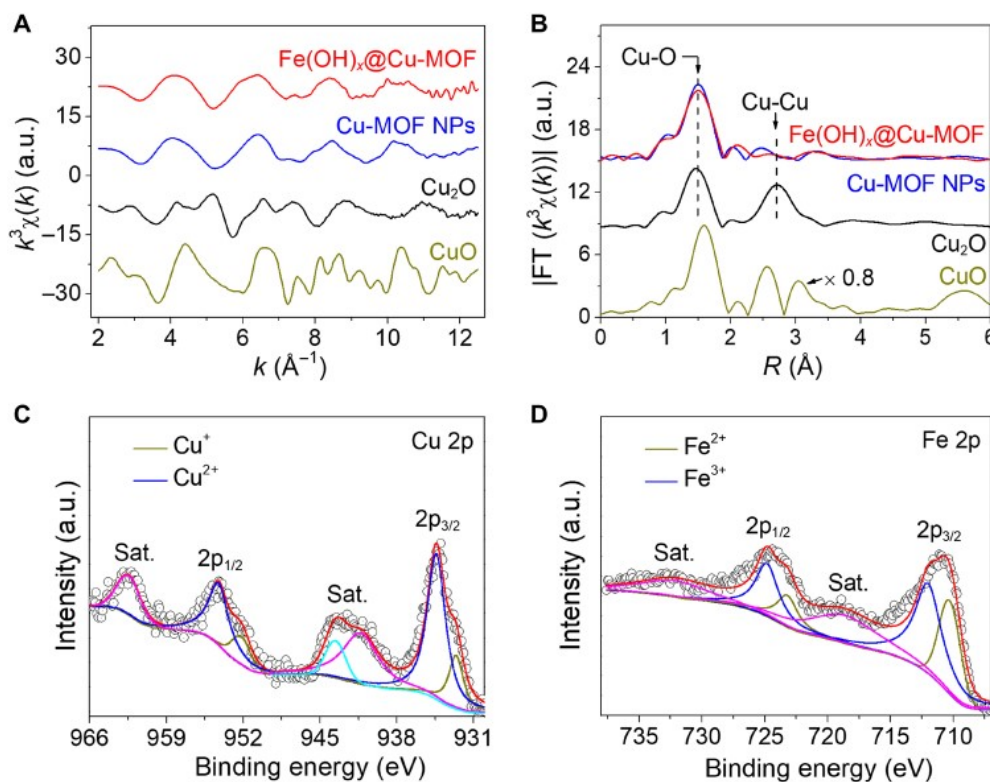


Fig. 3. XAFS and XPS characterizations. (A and B) The $k^3\chi(k)$ oscillation curves (A) and the Fourier transform curves (B) of Cu K -edge EXAFS spectra for CuO , Cu_2O , Cu-MOF NPs, and $\text{Fe(OH)}_x@\text{Cu-MOF}$ NBs. (C and D) Cu 2p XPS spectrum (C) and Fe 2p XPS spectrum (D) of $\text{Fe(OH)}_x@\text{Cu-MOF}$ NBs. a.u., arbitrary units.

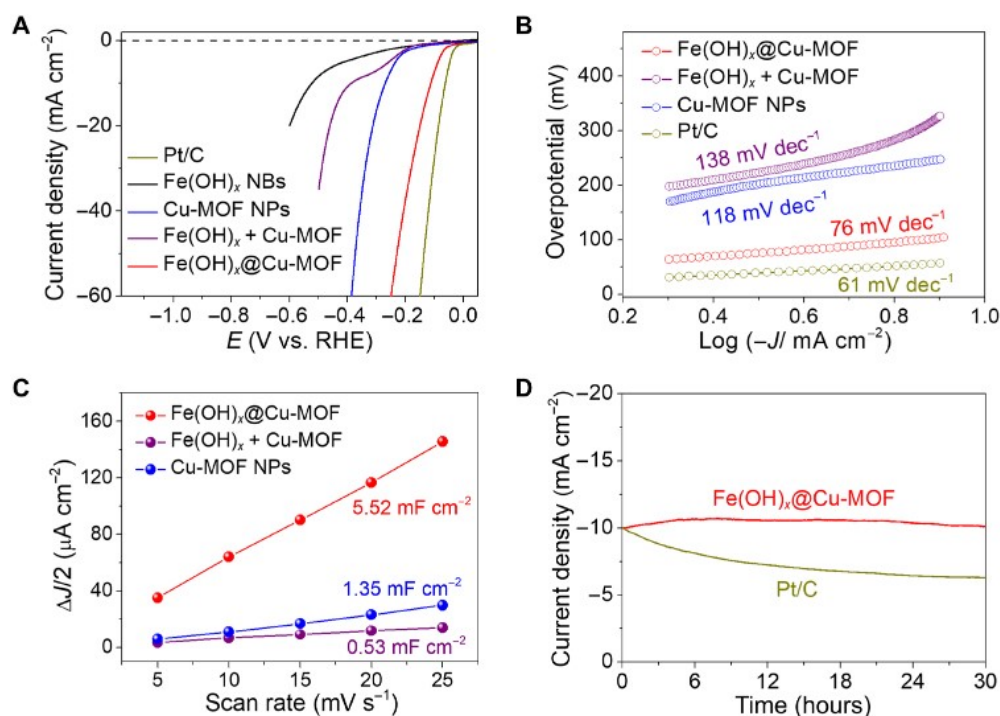


Fig. 4. Electrocatalytic performance. (A and B) LSV plots (A) and the corresponding Tafel slopes (B) of Pt/C, Fe(OH)_x NBs, Cu-MOF NPs, $\text{Fe(OH)}_x + \text{Cu-MOF}$, and $\text{Fe(OH)}_x@ \text{Cu-MOF}$ NBs. (C) Half of the capacitive current density ($\Delta j/2$) at 0.25 V versus RHE as a function of the scan rate for Cu-MOF NPs, $\text{Fe(OH)}_x + \text{Cu-MOF}$, and $\text{Fe(OH)}_x@ \text{Cu-MOF}$ NBs. (D) i - t curve for $\text{Fe(OH)}_x@ \text{Cu-MOF}$ NBs and Pt/C catalysts, where the applied potentials are -0.112 and -0.068 V versus RHE for $\text{Fe(OH)}_x@ \text{Cu-MOF}$ NBs and Pt/C catalysts, respectively.

(LSV) plots of $\text{Fe(OH)}_x@ \text{Cu-MOF}$ NBs. The $\text{Fe(OH)}_x@ \text{Cu-MOF}$ NBs catalyze HER at an onset potential (defined as the potential at -1.0 mA cm^{-2}) of about 0.04 V versus reversible hydrogen electrode (RHE) and then deliver a current density of -10 mA cm^{-2} at a small overpotential (η_{10}) of 112 mV, superior to that of Fe(OH)_x NBs (523 mV), Cu-MOF NPs (273 mV), and $\text{Fe(OH)}_x + \text{Cu-MOF}$ (391 mV). Moreover, as shown in Fig. 4B, a small Tafel slope of 76 mV dec^{-1} is obtained for $\text{Fe(OH)}_x@ \text{Cu-MOF}$ NBs, obviously outperforming that of Cu-MOF NPs (118 mV dec^{-1}) and $\text{Fe(OH)}_x + \text{Cu-MOF}$ (138 mV dec^{-1}), indicating faster HER kinetics of the former. In addition, $\text{Fe(OH)}_x@ \text{Cu-MOF}$ NBs exhibit a high turnover frequency (TOF) during HER with a typical value of about 0.39 s^{-1} at the overpotential of 100 mV, whereas both samples of $\text{Fe(OH)}_x + \text{Cu-MOF}$ and Cu-MOF NPs only show moderate TOF values at the level of about 0.01 s^{-1} (fig. S21). Notably, the HER activity trends of all samples are in the order of $\text{Fe(OH)}_x@ \text{Cu-MOF}$ NBs > Cu-MOF NPs > $\text{Fe(OH)}_x + \text{Cu-MOF}$ > Fe(OH)_x NBs. All these results suggest that the superior HER activity of $\text{Fe(OH)}_x@ \text{Cu-MOF}$ NBs is mainly from the ultrathin Cu-MOF layer, and the rational integration of Fe(OH)_x shell and Cu-MOF layer is quite beneficial for accelerating the HER kinetics in addition to the enhanced structural stability.

The electrochemical double-layer capacitance (C_{dl}) is calculated to estimate the electrochemically active surface area (ECSA) of $\text{Fe(OH)}_x@ \text{Cu-MOF}$ NBs, which is closely related to the number of exposed active sites (19, 42). As shown in Fig. 4C and fig. S22, $\text{Fe(OH)}_x@ \text{Cu-MOF}$ NBs exhibit the largest C_{dl} of 5.52 mF cm^{-2} , which is about 4 and 10 times, respectively, that of Cu-MOF NPs (1.35 mF cm^{-2}) and $\text{Fe(OH)}_x + \text{Cu-MOF}$ (0.53 mF cm^{-2}). This result suggests a high exposure of active sites in $\text{Fe(OH)}_x@ \text{Cu-MOF}$ NBs. Furthermore, the normalized LSV plots show superior HER

activity for $\text{Fe(OH)}_x@ \text{Cu-MOF}$ relative to Cu-MOF NPs and $\text{Fe(OH)}_x + \text{Cu-MOF}$ (fig. S23A), indicating the high intrinsic HER activity of the $\text{Cu}_1\text{-O}_2$ centers in $\text{Fe(OH)}_x@ \text{Cu-MOF}$ NBs. Moreover, according to the electrochemical impedance spectroscopy (EIS) results (fig. S23B), the smallest semicircle is observed for $\text{Fe(OH)}_x@ \text{Cu-MOF}$ NBs relative to Cu-MOF NPs and $\text{Fe(OH)}_x + \text{Cu-MOF}$, inferring apparent improvement in charge transfer. It is noteworthy that $\text{Fe(OH)}_x@ \text{Cu-MOF}$ NBs manifest robust long-term HER stability in alkaline solution, with negligible decay of the initial current density after a 30-hour HER test (Fig. 4D and fig. S24). In comparison, a total loss of about 30% of the initial current density is observed for the Pt/C catalyst. The NB architecture, as well as the hexagonal crystal structure of Cu-MOF, is well maintained after the long-term HER operation for $\text{Fe(OH)}_x@ \text{Cu-MOF}$ NBs (fig. S25), further confirming the excellent electrocatalytic stability. With the superior η_{10} , the small Tafel slope, and the high stability, these $\text{Fe(OH)}_x@ \text{Cu-MOF}$ NBs could be considered as one of the most active MOF-based HER electrocatalysts. The high-performance MOF-based HER electrocatalysts reported generally have η_{10} values of 50 to 160 mV with Tafel slopes of 40 to 100 mV dec^{-1} in alkaline solution (table S2) (14, 16, 44–49).

DISCUSSION

To shed light on the intrinsic electrocatalytic activity of $\text{Fe(OH)}_x@ \text{Cu-MOF}$ NBs, theoretical studies based on DFT calculations were carried out. From the structural models shown in Fig. 5A (see also figs. S26 and S27), Cu ions are coordinated with hydroxyl groups of HHTP linkers to form a honeycomb-like π -conjugated Cu-MOF layer (22, 34), where both coordinatively unsaturated $\text{Cu}_1\text{-O}_2$ and

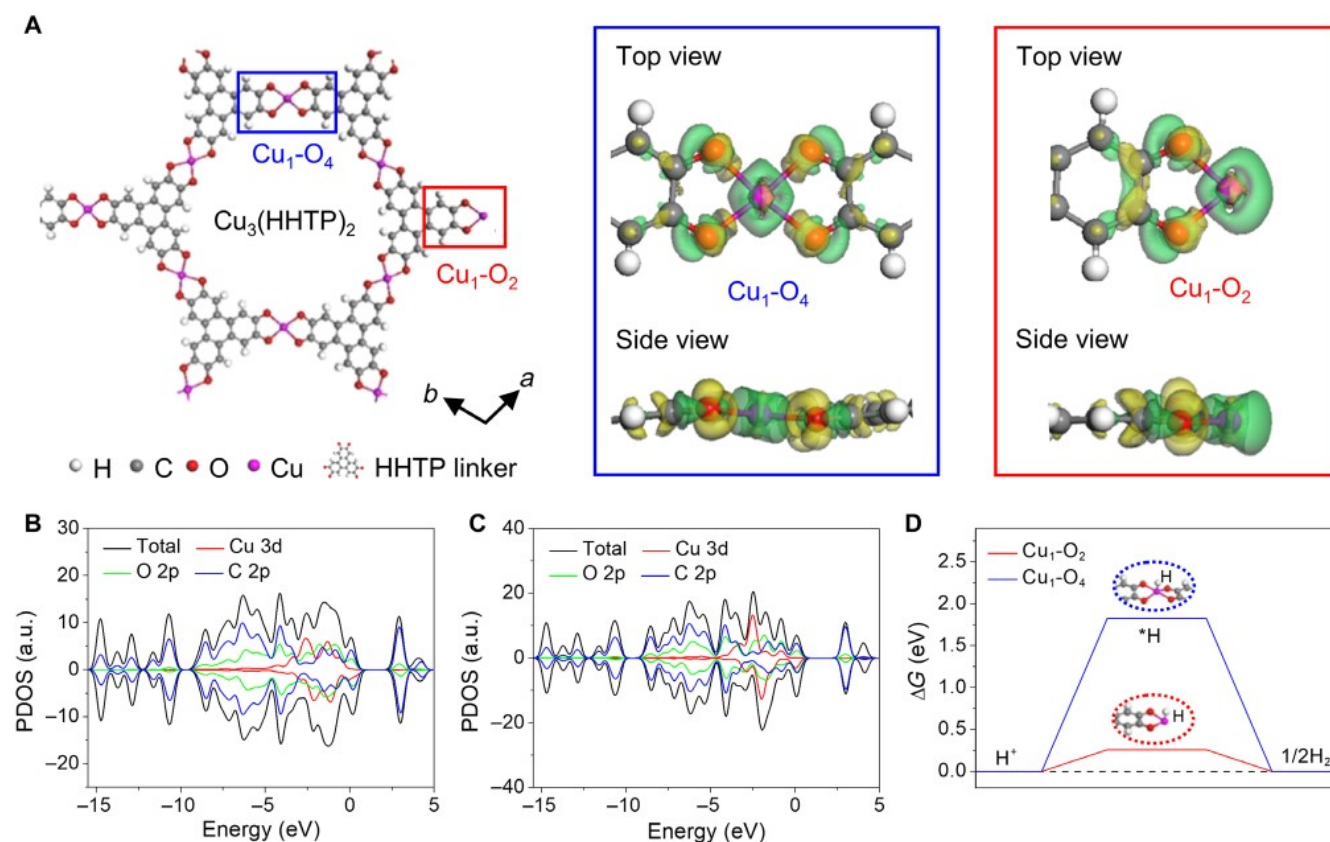


Fig. 5. DFT simulation. (A) Crystal structure of unsaturated Cu-MOF [$\text{Cu}_3(\text{HHTP})_2$] viewed along the c axis and the electron density difference plots of corresponding $\text{Cu}_1\text{-O}_4$ and $\text{Cu}_1\text{-O}_2$ centers, where yellow and green contours represent electron accumulation and depression, respectively. (B and C) Calculated partial density of states (PDOS) of Cu-MOF with (B) and without (C) $\text{Cu}_1\text{-O}_2$ centers. (D) Calculated free energy change of adsorbed $^*\text{H}$ on Cu sites of $\text{Cu}_1\text{-O}_4$ and $\text{Cu}_1\text{-O}_2$ centers.

saturated $\text{Cu}_1\text{-O}_4$ centers are observed for unsaturated Cu-MOF. It is intriguing that the $\text{Cu}_1\text{-O}_2$ center shows obvious local charge polarization along Cu-O-C bond relative to the $\text{Cu}_1\text{-O}_4$ one (Fig. 5A), in which asymmetric electron depletion region appears around the Cu atom and electron enrichment area locates over the adjacent O and C atoms. With the local electric polarization, it is thermodynamically favorable for the $\text{Cu}_1\text{-O}_2$ centers to strongly couple with H_2O molecules, and thus beneficial for dissociating the H-O bonds toward fast water reduction (50, 51). The calculated partial density of states (PDOS; Fig. 5, B and C) shows an asymmetric spin-up and spin-down electron density over the energy range of -5 to 0 eV for both saturated and unsaturated Cu-MOF, indicating their intrinsically conductive nature (14, 16). It is noteworthy that in the presence of unsaturated $\text{Cu}_1\text{-O}_2$ centers, a new strong PDOS peak of Cu 3d is observed around -1.0 eV, suggesting more energy levels of Cu 3d atomic orbitals for higher chemical redox capability (52, 53). The free energy of hydrogen adsorption (ΔG^*_H), a critical descriptor for HER activity (9, 16), is calculated to further assess the electrocatalytic activity of saturated $\text{Cu}_1\text{-O}_4$ and unsaturated $\text{Cu}_1\text{-O}_2$ centers. As shown in Fig. 5D, the ΔG^*_H over Cu sites of saturated $\text{Cu}_1\text{-O}_4$ centers is up to 1.83 eV, which means a large uphill energy barrier for the effective adsorption of surface $^*\text{H}$. In vast contrast, the ΔG^*_H over Cu sites of unsaturated $\text{Cu}_1\text{-O}_2$ centers is decreased drastically to 0.26 eV, thus thermodynamically favoring the $^*\text{H}$ formation toward fast HER kinetics. The above calculation results suggest that these unsaturated $\text{Cu}_1\text{-O}_2$ centers could act as intrinsic active centers

for effectively dissociating adsorbed H_2O molecules into key $^*\text{H}$ intermediates, thus endowing unsaturated Cu-MOF with high HER activity.

Apart from the $\text{Cu}_1\text{-O}_2$ active centers, the well-designed hollow structure is also very important for the improved HER performance of $\text{Fe}(\text{OH})_x/\text{Cu-MOF}$ NBs. Specifically, the NB structure with large surface area could expose numerous active centers of the nanoscale Cu-MOF on the surface of $\text{Fe}(\text{OH})_x$, as verified by capacitance results in Fig. 4C and fig. S22, which directly and effectively enhances the electrocatalytic HER performance. In addition, the tight connection between the $\text{Fe}(\text{OH})_x$ inner shell and the Cu-MOF outer layer is very helpful for lowering the charge transfer barrier during the HER process, as corroborated by the aforementioned EIS analyses (fig. S23B). With the lower charge transfer barrier, the HER kinetics of $\text{Fe}(\text{OH})_x/\text{Cu-MOF}$ NBs would be substantially accelerated. Moreover, the robust $\text{Fe}(\text{OH})_x$ inner shell could also guarantee the structural stability for the long-term HER operation, as confirmed by the stability tests (Fig. 4D and figs. S24 and S25). As a result, with the merits of highly exposed active $\text{Cu}_1\text{-O}_2$ centers, enhanced charge transfer, and robust structure, the synthesized $\text{Fe}(\text{OH})_x/\text{Cu-MOF}$ NBs have manifested excellent HER performance with high activity and superior stability in alkaline solution.

In summary, a nanoscale layer of conductive Cu-MOFs has been rationally supported on iron hydr(oxy)oxide [$\text{Fe}(\text{OH})_x$] NBs as a promising electrocatalyst for electrochemical hydrogen evolution. The rational synthesis involves a facile template-engaged solvothermal

reaction and subsequent redox-etching strategy. Synchrotron radiation characterizations and theoretical calculations reveal that the highly exposed coordinatively unsaturated $\text{Cu}_1\text{-O}_2$ centers are beneficial for the generation of $^*\text{H}$ intermediates toward fast HER kinetics, which is mainly responsible for the improved HER performance of the synthesized $\text{Fe}(\text{OH})_x\text{@Cu-MOF}$ NBs. This work may offer some new inspiration for design and synthesis of advanced cost-effective MOF-based electrocatalysts toward efficient energy conversion and storage.

MATERIALS AND METHODS

Synthesis of Cu_2O nanocubes

In a typical process, 375 mg of $\text{CuSO}_4\cdot 5\text{H}_2\text{O}$ and 147 mg of sodium citrate tribasic dihydrate were dissolved into 80 ml of deionized (DI) water and then kept under stirring for 15 min. Subsequently, 20 ml (1 g, 1.25 M) of NaOH aqueous solution was added into the above solution, followed by addition of 50 ml (264 mg, 0.03 M) of L-ascorbic acid aqueous solution after stirring for another 15 min. Afterward, the obtained solution was continuously stirred for 3 min and then aged for 1 hour at room temperature. The Cu_2O nanocubes were obtained by centrifugation and washed with DI water and ethanol for five times.

Synthesis of Cu_2O supported conductive Cu-MOF ($\text{Cu}_2\text{O@Cu-MOF}$) core-shell nanocubes

In a typical preparation, 5 mg of Cu_2O nanocubes was dispersed into a mixed solution of 8 ml of *N,N*-dimethylformamide (DMF) and 300 μl of DI water by ultrasonication for 30 min, followed by addition of 2 ml of DMF solution containing 4 mg of HHTP ligands. After stirring for 5 min, the above solution was transferred to a preheated oil bath and then kept at 120°C for 5 min under stirring. The $\text{Cu}_2\text{O@Cu-MOF}$ core-shell nanocubes were harvested by centrifugation and washed with DMF and methanol for five times.

Synthesis of $\text{Fe}(\text{OH})_x\text{@Cu-MOF}$ NBs

$\text{Cu}_2\text{O@Cu-MOF}$ nanocubes (2.5 mg) were dispersed into a mixed solution of 20 ml of DMF and 2 ml of DI water by ultrasonication for 1 hour, followed by addition of 20 ml of DMF solution containing 17.8 mg of anhydrous FeCl_3 under stirring. Subsequently, this resultant solution was continuously stirred at room temperature for 4 hours. The $\text{Fe}(\text{OH})_x\text{@Cu-MOF}$ NBs were obtained by centrifugation and washed with DMF and methanol for five times.

Synthesis of bulk conductive Cu-MOF NPs

Copper acetate monohydrate (12 mg) was dissolved into a mixed solution of 5 ml of DMF and 1 ml of DI water, followed by addition of 5 ml of DMF solution containing 13 mg of HHTP ligands under stirring. After stirring for 5 min, the resultant solution was transferred to oil bath and kept at 120°C for 2 hours. The Cu-MOF NPs were obtained by centrifugation and washed with DMF and DI water for several times.

Synthesis of $\text{Fe}(\text{OH})_x$ NBs

Cu_2O nanocubes (5 mg) were dispersed into 39 ml of ethanol by ultrasonication for 30 min, followed by addition of 1.0 ml of 1.71 M NaCl aqueous solution. Subsequently, 10 ml of ethanol solution containing 8.9 mg of anhydrous FeCl_3 was added dropwise into the above solution under stirring. The resultant solution was continuously

stirred at room temperature for 30 min. Last, the $\text{Fe}(\text{OH})_x$ NBs were obtained by centrifugation and washed with DI water and ethanol for several times.

Materials characterizations

The morphology of the samples was examined by FESEM (JEOL-6700) and TEM (JEOL, JEM-2100). The crystal structure of the samples was examined by XRD on the Bruker D2 Phaser X-Ray Diffractometer with Cu K_α radiation ($\lambda = 1.5406 \text{ \AA}$). The theoretical XRD pattern of conductive Cu-MOF was calculated on the basis of the XRD simulation software of Mercury 4.1.0. The compositions of the samples were analyzed by the FESEM instrument equipped with an EDX spectroscopy. The elemental mapping images of the samples were measured by using the EDX spectroscopy attached to TEM (JEOL, JEM-2100F). The nitrogen adsorption-desorption isothermal curves of the samples were obtained at 77 K by using BELSORP-mini (MicrotracBEL Corp.) The electronic structure of the samples was studied by XPS (PHI Quantum 2000) with the adventitious carbon (C 1s) at the binding energy of 284.6 eV as the reference. The surface functional groups of the samples were determined by FTIR (Thermo-Smart-ITR). The XAFS spectroscopy of Cu and/or Fe *K*-edge was collected at the X-ray absorption fine structure for catalysis (XAFCA) beamline of the Singapore Synchrotron Light Source (SSLS), Singapore. The energy was calibrated using a copper foil. Quantitative curve fittings of the Fourier-transformed $k^3\chi(k)$ in the *R*-space were carried out on the basis of the ARTEMIS module implemented in the IFEFFIT software packages.

Electrochemical measurements

The electrochemical tests of the samples were evaluated in a three-electrode configuration workstation (CHI 660E), with Hg/HgO and graphite rod as the reference and counter electrodes, respectively. The automatic *iR* compensation (*i* and *R* mean the corresponding compensated current and resistance, respectively) with 90% compensated level was used for the electrochemical measurements. To prepare the catalyst ink, 5 mg of catalyst was dispersed into a mixed solution of water (0.25 ml), ethanol (0.70 ml), and 0.5 weight % Nafion solution (0.05 ml), followed by ultrasonication for 30 min. The catalytic ink was loaded onto a 1 cm by 3 cm carbon paper as the working electrode, with an effective loading area of 1 cm by 1 cm. Typically, 20 μl of catalytic ink was dropped on the carbon paper electrode and then dried at room temperature. LSV curves were measured in alkaline (1.0 M KOH) solutions at a scan rate of 5 mV s^{-1} . All potentials were converted to RHE potentials based on Nernst equation: $E_{\text{RHE}} = E_{\text{Hg/HgO}} + 0.098 + 0.059 \times \text{pH}$. The overpotential (η) for hydrogen evolution was calculated according to the following formula: $\eta = 0 - E_{\text{RHE}}$ V. The ECSA of samples was evaluated by measuring the electrochemical double-layer capacitance (C_{dl}) under the potential range of 0.2 to 0.3 V versus RHE. The EIS test was recorded under a frequency range of 0.1 to 10^5 Hz with an amplitude of 5 mV. For the $2e^-$ HER process, the formula $\text{TOF} = (j \times A) / (2 \times F \times m)$ was used to calculate the TOF values for catalysts, where *j*, *A*, *F*, and *m* are the current density at a given potential, the surface of the electrode, the faradaic constant, and the number of moles of metal on the electrode, respectively. The loading mass of active metal components was tested by ICP-OES for various electrodes. On the basis of the HER LSV measurement results, Cu species served as the real HER active sites among the potentials of -0.3 to 0 V versus RHE for $\text{Fe}(\text{OH})_x\text{@Cu-MOF}$ NBs, $\text{Fe}(\text{OH})_x$ + Cu-MOF, and Cu-MOF NP

catalysts. Accordingly, only the loading mass of Cu species was included into the TOF calculation for different catalysts in the potential ranges of -0.3 to 0 V.

DFT calculations

The theoretical calculations were conducted on the basis of the first-principles DFT calculations by using the Vienna Ab-initio Simulation package and Ambridge Sequential Total Energy package. The generalized-gradient approximation was used to describe the electronic exchange-correlation potential. The energy cutoff was set to 400 eV, and the atomic positions were allowed to relax until the energy and forces were less than 10^{-4} eV/atom and 10^{-2} eV/Å, respectively. The unsaturated Cu-MOF layer was modeled in supercell geometry containing seven HHTP linkers coordinated with 11 Cu nodes, where the molar ratio of $\text{Cu}_1\text{-O}_2$ to $\text{Cu}_1\text{-O}_4$ is about 0.2:1. The hydrogen adsorption free energy (ΔG^*_H) was calculated as follows: $\Delta G^*_\text{H} = \Delta E^*_\text{H} + \Delta E_{\text{ZPE}} - T\Delta S^*_\text{H}$, where ΔE^*_H is the adsorption energy of $^*\text{H}$, ΔE_{ZPE} is the change of zero-point energy, T is the temperature of 298.15 K, and ΔS^*_H is the change of entropy. Especially, ΔE^*_H is defined as follows: $\Delta E^*_\text{H} = E_{\text{total}} - E_{\text{catalyst}} - 1/2E_{\text{H}_2}$, where E_{total} , E_{catalyst} , and E_{H_2} are the total energy of catalyst with adsorbed H, the energy of isolated catalyst, and the energy of H_2 molecule in the gas phase, respectively.

SUPPLEMENTARY MATERIALS

Supplementary material for this article is available at <http://advances.sciencemag.org/cgi/content/full/7/18/eabg2580/DC1>

REFERENCES AND NOTES

- J. B. Zimmerman, P. T. Anastas, H. C. Erythropel, W. Leitner, Designing for a green chemistry future. *Science* **367**, 397–400 (2020).
- H. Zhang, L. Yu, T. Chen, W. Zhou, X. W. Lou, Surface modulation of hierarchical MoS_2 nanosheets by Ni single atoms for enhanced electrocatalytic hydrogen evolution. *Adv. Funct. Mater.* **28**, 1807086 (2018).
- J. Zhu, L. Hu, P. Zhao, L. Y. S. Lee, K.-Y. Wong, Recent advances in electrocatalytic hydrogen evolution using nanoparticles. *Chem. Rev.* **120**, 851–918 (2020).
- H. Zhang, J. Nai, L. Yu, X. W. Lou, Metal-organic-framework-based materials as platforms for renewable energy and environmental applications. *Joule* **1**, 77–107 (2017).
- X. F. Lu, L. Yu, J. Zhang, X. W. Lou, Ultrafine dual-phased carbide nanocrystals confined in porous nitrogen-doped carbon dodecahedrons for efficient hydrogen evolution reaction. *Adv. Mater.* **31**, 1900699 (2019).
- Z. W. Seh, J. Kibsgaard, C. F. Dickens, I. Chorkendorff, J. K. Nørskov, T. F. Jaramillo, Combining theory and experiment in electrocatalysis: Insights into materials design. *Science* **355**, eaad4998 (2017).
- H. Zhang, P. An, W. Zhou, B. Y. Guan, P. Zhang, J. Dong, X. W. Lou, Dynamic traction of lattice-confined platinum atoms into mesoporous carbon matrix for hydrogen evolution reaction. *Sci. Adv.* **4**, eaao6657 (2018).
- K. Jiang, B. Liu, M. Luo, S. Ning, M. Peng, Y. Zhao, Y. R. Lu, T. S. Chan, F. M. F. de Groot, Y. Tan, Single platinum atoms embedded in nanoporous cobalt selenide as electrocatalyst for accelerating hydrogen evolution reaction. *Nat. Commun.* **10**, 1743 (2019).
- X. F. Lu, L. Yu, X. W. Lou, Highly crystalline Ni-doped FeP/carbon hollow nanorods as all-pH efficient and durable hydrogen evolving electrocatalysts. *Sci. Adv.* **5**, eaav6009 (2019).
- Y. Yang, Y. Qian, H. Li, Z. Zhang, Y. Mu, D. Do, B. Zhou, J. Dong, W. Yan, Y. Qin, L. Fang, R. Feng, J. Zhou, P. Zhang, J. Dong, G. Yu, Y. Liu, X. Zhang, X. Fan, O-coordinated W-Mo dual-atom catalyst for pH-universal electrocatalytic hydrogen evolution. *Sci. Adv.* **6**, eaab6586 (2020).
- H. Zhang, W. Zhou, X. F. Lu, T. Chen, X. W. Lou, Implanting isolated Ru atoms into edge-rich carbon matrix for efficient electrocatalytic hydrogen evolution. *Adv. Energy Mater.* **10**, 2000882 (2020).
- Q. Qiu, T. Wang, L. Jing, K. Huang, D. Qin, Tetra-carboxylic acid based metal-organic framework as a high-performance bifunctional electrocatalyst for HER and OER. *Int. J. Hydrogen Energy* **45**, 11077–11088 (2020).
- X. Chen, S. Huang, F. Sun, N. Lai, Modifications of metal and ligand to modulate the oxygen reduction reaction activity of two-dimensional MOF catalysts. *J. Phys. Chem. C* **124**, 1413–1420 (2019).
- L. S. Xie, G. Skorupskii, M. Dincă, Electrically conductive metal-organic frameworks. *Chem. Rev.* **120**, 8536–8580 (2020).
- M. Hmadeh, Z. Lu, Z. Liu, F. Gándara, H. Furukawa, S. Wan, V. Augustyn, R. Chang, L. Liao, F. Zhou, E. Perre, V. Ozolins, K. Suenaga, X. Duan, B. Dunn, Y. Yamamoto, O. Terasaki, O. M. Yaghi, New porous crystals of extended metal-catecholates. *Chem. Mater.* **24**, 3511–3513 (2012).
- H. Huang, Y. Zhao, Y. Bai, F. Li, Y. Zhang, Y. Chen, Conductive metal-organic frameworks with extra metallic sites as an efficient electrocatalyst for the hydrogen evolution reaction. *Adv. Sci.* **7**, 2000012 (2020).
- Y. H. Budnikova, Recent advances in metal-organic frameworks for electrocatalytic hydrogen evolution and overall water splitting reactions. *Dalton Trans.* **49**, 12483–12502 (2020).
- H. Xu, B. Fei, G. Cai, Y. Ha, J. Liu, H. Jia, J. Zhang, M. Liu, R. Wu, Boronization-induced ultrathin 2D nanosheets with abundant crystalline-amorphous phase boundary supported on nickel foam toward efficient water splitting. *Adv. Energy Mater.* **10**, 1902714 (2019).
- W. Cheng, X. F. Lu, D. Luan, X. W. Lou, NiMn-based bimetal-organic framework nanosheets supported on multi-channel carbon fibers for efficient oxygen electrocatalysis. *Angew. Chem. Int. Ed.* **59**, 18234–18239 (2020).
- F. Sun, X. Chen, Oxygen reduction reaction on $\text{Ni}_3(\text{HITP})_2$: A catalytic site that leads to high activity. *Electrochem. Commun.* **82**, 89–92 (2017).
- D. Feng, T. Lei, M. R. Lukatskaya, J. Park, Z. Huang, M. Lee, L. Shaw, S. Chen, A. A. Yakovenko, A. Kulkarni, J. Xiao, K. Fredrickson, J. B. Tok, X. Zou, Y. Cui, Z. Bao, Robust and conductive two-dimensional metal-organic frameworks with exceptionally high volumetric and areal capacitance. *Nat. Energy* **3**, 30–36 (2018).
- K. W. Nam, S. S. Park, R. dos Reis, V. P. Dravid, H. Kim, C. A. Mirkin, J. F. Stoddart, Conductive 2D metal-organic framework for high-performance cathodes in aqueous rechargeable zinc batteries. *Nat. Commun.* **10**, 4948 (2019).
- M. Ko, L. Mendecki, K. A. Mirica, Conductive two-dimensional metal-organic frameworks as multifunctional materials. *Chem. Commun.* **54**, 7873–7891 (2018).
- L. Guo, J. Sun, J. Wei, Y. Liu, L. Hou, C. Yuan, Conductive metal-organic frameworks: Recent advances in electrochemical energy-related applications and perspectives. *Carbon Energy* **2**, 203–222 (2020).
- A. J. Clough, J. W. Yoo, M. H. Mecklenburg, S. C. Marinescu, Two-dimensional metal-organic surfaces for efficient hydrogen evolution from water. *J. Am. Chem. Soc.* **137**, 118–121 (2015).
- N. Lahiri, N. Lotfizadeh, R. Tsuchikawa, V. V. Deshpande, J. Louie, Hexaaminobenzene as a building block for a family of 2D coordination polymers. *J. Am. Chem. Soc.* **139**, 19–22 (2017).
- H. Wang, Q.-L. Zhu, R. Zou, Q. Xu, Metal-organic frameworks for energy applications. *Chem* **2**, 52–80 (2017).
- L. Yu, J. F. Yang, B. Y. Guan, Y. Lu, X. W. Lou, Hierarchical hollow nanoprisms based on ultrathin Ni-Fe layered double hydroxide nanosheets with enhanced electrocatalytic activity towards oxygen evolution. *Angew. Chem. Int. Ed.* **57**, 172–176 (2018).
- G. Chen, H. Wan, W. Ma, N. Zhang, Y. Cao, X. Liu, J. Wang, R. Ma, Layered metal hydroxides and their derivatives: Controllable synthesis, chemical exfoliation, and electrocatalytic applications. *Adv. Energy Mater.* **10**, 1902535 (2019).
- Z.-P. Wu, X. F. Lu, S.-Q. Zang, X. W. Lou, Non-noble-metal-based electrocatalysts toward the oxygen evolution reaction. *Adv. Funct. Mater.* **30**, 1910274 (2020).
- W. Ahn, M. G. Park, D. U. Lee, M. H. Seo, G. Jiang, Z. P. Cano, F. M. Hassan, Z. Chen, Hollow multivoid nanocuboids derived from ternary Ni-Co-Fe prussian blue analog for dual-electrocatalysis of oxygen and hydrogen evolution reactions. *Adv. Funct. Mater.* **28**, 1802129 (2018).
- Z. Wang, D. Luan, C. M. Li, F. Su, S. Madhavi, F. Y. C. Boey, X. W. Lou, Engineering nonspherical hollow structures with complex interiors by template-engaged redox etching. *J. Am. Chem. Soc.* **132**, 16271–16277 (2010).
- Y. Fang, D. Luan, Y. Chen, S. Y. Gao, X. W. Lou, Rationally designed three-layered $\text{Cu}_2\text{S}@ \text{carbon}@ \text{MoS}_2$ hierarchical nanoboxes for efficient sodium storage. *Angew. Chem. Int. Ed.* **59**, 7178–7183 (2020).
- W. H. Li, K. Ding, H. R. Tian, M. S. Yao, B. Nath, W. H. Deng, Y. Wang, G. Xu, Conductive metal-organic framework nanowire array electrodes for high-performance solid-state supercapacitors. *Adv. Funct. Mater.* **27**, 1702067 (2017).
- H. Su, W. Zhou, H. Zhang, W. Zhou, X. Zhao, Y. Li, M. Liu, W. Cheng, Q. Liu, Dynamic evolution of solid-liquid electrochemical interfaces over single-atom active sites. *J. Am. Chem. Soc.* **142**, 12306–12313 (2020).
- F. Tang, H. Su, X. Zhao, H. Zhang, F. Hu, P. Yao, Q. Liu, W. Cheng, Potential-driven surface active structure rearrangement over $\text{FeP}@ \text{NC}$ towards efficient electrocatalytic hydrogen evolution. *Phys. Chem. Chem. Phys.* **21**, 7918–7923 (2019).

37. T. Zhang, X. Nie, W. Yu, X. Guo, C. Song, R. Si, Y. Liu, Z. Zhao, Single atomic Cu-N₂ catalytic sites for highly active and selective hydroxylation of benzene to phenol. *iScience* **22**, 97–108 (2019).
38. J. Jiao, R. Lin, S. Liu, W. C. Cheong, C. Zhang, Z. Chen, Y. Pan, J. Tang, K. Wu, S. F. Hung, H. M. Chen, L. Zheng, Q. Lu, X. Yang, B. Xu, H. Xiao, J. Li, D. Wang, Q. Peng, C. Chen, Y. Li, Copper atom-pair catalyst anchored on alloy nanowires for selective and efficient electrochemical reduction of CO₂. *Nat. Chem.* **11**, 222–228 (2019).
39. H. Su, X. Zhao, W. Cheng, H. Zhang, Y. Li, W. Zhou, M. Liu, Q. Liu, Hetero-N-coordinated Co single sites with high turnover frequency for efficient electrocatalytic oxygen evolution in an acidic medium. *ACS Energy Lett.* **4**, 1816–1822 (2019).
40. E. M. Miner, S. Gul, N. D. Ricke, E. Pastor, J. Yano, V. K. Yachandra, T. van Voorhis, M. Dincă, Mechanistic evidence for ligand-centered electrocatalytic oxygen reduction with the conductive MOF Ni₃(hexaiminotriphenylene)₂. *ACS Catal.* **7**, 7726–7731 (2017).
41. W. Cheng, X. Zhao, H. Su, F. Tang, W. Che, H. Zhang, Q. Liu, Lattice-strained metal-organic-framework arrays for bifunctional oxygen electrocatalysis. *Nat. Energy* **4**, 115–122 (2019).
42. J. K. Liu, W. Cheng, F. Tang, H. Su, Y. Huang, F. Hu, X. Zhao, Y. Jiang, Q. Liu, S. Wei, Electron delocalization boosting highly efficient electrocatalytic water oxidation in layered hydrotalcites. *J. Phys. Chem. C* **121**, 21962–21968 (2017).
43. M. Nie, Y. Li, J. He, C. Xie, Z. Wu, B. Sun, K. Zhang, L. Kong, J. Liu, Degradation of tetracycline in water using Fe₃O₄ nanospheres as Fenton-like catalysts: Kinetics, mechanisms and pathways. *New J. Chem.* **44**, 2847–2857 (2020).
44. H. W. Lin, D. Senthil Raja, X. F. Chuah, C. T. Hsieh, Y. A. Chen, S. Y. Lu, Bi-metallic MOFs possessing hierarchical synergistic effects as high performance electrocatalysts for overall water splitting at high current densities. *Appl. Catal. Environ.* **258**, 118023 (2019).
45. J. Duan, S. Chen, C. Zhao, Ultrathin metal-organic framework array for efficient electrocatalytic water splitting. *Nat. Commun.* **8**, 15341 (2017).
46. Z. Chen, B. Fei, M. Hou, X. Yan, M. Chen, H. Qing, R. Wu, Ultrathin prussian blue analogue nanosheet arrays with open bimetal centers for efficient overall water splitting. *Nano Energy* **68**, 104371 (2020).
47. T. Liu, P. Li, N. Yao, T. Kong, G. Cheng, S. Chen, W. Luo, Self-sacrificial template-directed vapor-phase growth of MOF assemblies and surface vulcanization for efficient water splitting. *Adv. Mater.* **31**, 1806672 (2019).
48. M. Liu, W. Zheng, S. Ran, S. T. Boles, L. Y. S. Lee, Overall water-splitting electrocatalysts based on 2D CoNi-metal-organic frameworks and its derivative. *Adv. Mater. Interfaces* **5**, 1800849 (2018).
49. D. Senthil Raja, X. F. Chuah, S. Y. Lu, In situ grown bimetallic MOF-based composite as highly efficient bifunctional electrocatalyst for overall water splitting with ultrastability at high current densities. *Adv. Energy Mater.* **8**, 1801065 (2018).
50. P. F. Liu, H. Yin, H. Q. Fu, M. Y. Zu, H. G. Yang, H. Zhao, Activation strategies of water-splitting electrocatalysts. *J. Mater. Chem. A* **8**, 10096–10129 (2020).
51. C. Lei, Y. Wang, Y. Hou, P. Liu, J. Yang, T. Zhang, X. Zhuang, M. Chen, B. Yang, L. Lei, C. Yuan, M. Qiug, X. Feng, Efficient alkaline hydrogen evolution on atomically dispersed Ni-N₄ species anchored porous carbon with embedded Ni nanoparticles by accelerating water dissociation kinetics. *Energy Environ. Sci.* **12**, 149–156 (2019).
52. J.-H. Song, G. Yoon, B. Kim, D. Eum, H. Park, D.-H. Kim, K. Kang, Anionic redox activity regulated by transition metal in lithium-rich layered oxides. *Adv. Energy Mater.* **10**, 2001207 (2020).
53. D. A. Kuznetsov, B. Han, Y. Yu, R. R. Rao, J. Hwang, Y. Román-Leshkov, Y. Shao-Horn, Tuning redox transitions via inductive effect in metal oxides and complexes, and implications in oxygen electrocatalysis. *Joule* **2**, 225–244 (2018).

Acknowledgments: We thank S. Xi and the X-ray absorption fine structure for catalysis (XAFCA) beamline of the Singapore Synchrotron Light Source (SSLS) for supporting the XAFS measurements. **Funding:** X.W.L. acknowledges the funding support from the Ministry of Education of Singapore through the Academic Research Fund (AcRF) Tier-2 funding (MOE2019-T2-2-049) and the National Research Foundation (NRF) of Singapore via the NRF Investigatorship (NRF-NRFI2016-04). **Author contributions:** W.C. and X.W.L. conceived the idea. W.C. carried out the materials synthesis. W.C. and H.Z. carried out materials characterizations and analyzed the experimental data. W.C., D.L., and X.W.L. discussed the results and cowrote the manuscript. All authors read and commented on the manuscript. **Competing interests:** The authors declare that they have no competing interests. **Data and materials availability:** All data needed to evaluate the conclusions in the paper are present in the paper and/or the Supplementary Materials. Additional data related to this paper may be requested from the authors.

Submitted 21 December 2020

Accepted 10 March 2021

Published 28 April 2021

10.1126/sciadv.abg2580

Citation: W. Cheng, H. Zhang, D. Luan, X. W. Lou, Exposing unsaturated Cu₁-O₂ sites in nanoscale Cu-MOF for efficient electrocatalytic hydrogen evolution. *Sci. Adv.* **7**, eabg2580 (2021).